Journal of Biomechanics 94 (2019) 170–179

Contents lists available at ScienceDirect

Journal of Biomechanics

journal homepage: www.elsevier.com/locate/jbiomech
www.JBiomech.com

In-stent graft helical flow intensity reduces the risk of migration after endovascular aortic repair

Paola Tasso [a,1], Maurizio Lodi Rizzini [a,1], Anastasios Raptis [b], Mitialdis Matsagkas [c], Giuseppe De Nisco [a], Diego Gallo [a], Michalis Xenos [d], Umberto Morbiducci [a,*]

[a] PolitoBIOMed Lab, Department of Mechanical and Aerospace Engineering, Politecnico di Torino, Torino, Italy
[b] Laboratory for Vascular Simulations, Institute of Vascular Diseases, Larissa, Greece
[c] Department of Vascular Surgery, Faculty of Medicine, University of Thessaly, Larissa, Greece
[d] Department of Mathematics University of Ioannina, Ioannina, Greece

ARTICLE INFO

Article history:
Accepted 27 July 2019

Keywords:
Abdominal aortic aneurysm
Displacement forces
Helical flow
Computational fluid dynamics
Power losses

ABSTRACT

During the last years endovascular aneurysm repair (EVAR) became the elective treatment for abdominal aortic aneurysms (AAAs) thanks to lower mortality and morbidity rates than open surgery. In face of these advantages, stent-graft performances are still clinically suboptimal. In particular, post-surgical complications derive from device migration as a consequence of the hemodynamic forces acting on the endograft. In this regard, while the importance of hemodynamic surface forces is well recognized, the role of the in-stent flow is still unclear. Here we hypothesize that in-stent helical blood flow patterns might influence the distribution of the displacement forces (**DF**s) acting on the stent-graft and, ultimately, the risk of stent migration. To test this hypothesis, the hemodynamics of 20 post-EVAR models of patients treated with two different commercial endografts was analyzed using computational hemodynamics.

The main findings of the study indicate that: (1) helical flow intensity decreases the risk of endograft migration, as given by an inverse correlation between helicity intensity (h_2) and time-averaged displacement forces (**TADF**s) ($p < 0.05$); (2) unbalanced counter-rotating helical structures in the legs of the device contribute, in particular along the systole, to significantly suppress **TADF**s ($p < 0.01$); (3) as expected, helical flow intensity is positively correlated with pressure drop and resistance to flow ($p < 0.001$). The findings of this study suggest that a design strategy promoting in-stent helical flow structures could contribute to minimize the risk of migration of implanted EVAR devices.

1. Introduction

Abdominal aortic aneurysm (AAA) is a vascular pathology consisting in the irreversible enlargement of the abdominal aorta lumen as a consequence of the degradation of the structural and mechanical properties of the vessel wall (Ailawadi et al., 2003). If untreated, AAA could rupture, causing internal hemorrhage that can be accompanied with catastrophic outcomes. In the last decades, endovascular aneurysm repair (EVAR) has become the elective treatment for AAA (Budtz-Lilly et al., 2017; Chang et al., 2013; Powell et al., 2017). EVAR is a minimally invasive procedure that involves the endovascular insertion of a stent graft device which excludes the aneurismal sac from blood flow, reducing the risk of rupture. Given the low morbidity and mortality rates, and quick recovery, EVAR is considered an efficient alternative to open surgery (Kontopodis et al., 2015; Sweeting et al., 2015; Winterborn et al., 2009). In face of these advantages, EVAR presents post-surgical complications, like endoleaks, thrombosis and migration (Bastos et al., 2010; Daye et al., 2018; Desai et al., 2010; Van Marrewijk et al., 2005). The estimated average re-intervention rate of 11% after two years (Kent et al., 2018) reveals that there is much room for improvement of endografts design.

In particular, stent graft migration is a critical post-EVAR complication (Kent et al., 2018; Turney et al., 2014) that can further induce type I endoleak, markedly increasing the threat of AAA rupture and the requirement for urgent corrective treatment (Mohan et al., 2002). The main factors contributing to stent graft migration derive from displacement forces acting on the device that depend

* Corresponding author at: PolitoBIOMed Lab, Department of Mechanical and Aerospace Engineering, Politecnico di Torino, Corso Duca degli Abruzzi 24, 10129 Turin, Italy.
E-mail address: umberto.morbiducci@polito.it (U. Morbiducci).
[1] P. Tasso and M. Lodi Rizzini contributed equally to this study.

https://doi.org/10.1016/j.jbiomech.2019.07.034
0021-9290/

on hemodynamics and anatomy (Figueroa et al., 2009; Tasso et al., 2018). Technically, an implanted stent graft is subject to forces exerted by blood on its internal surface along the cardiac cycle, and these hemodynamic forces could contribute to endograft migration. To achieve persistent fixation, some stent-graft devices take advantage of hooks-based anchorage systems (Morris et al., 2016). However, the risk of failure is not fully dodged with the implementation of sophisticated fixation systems, as migration is still possible after EVAR even with new generation endovascular devices.

While hemodynamic surface forces at the endograft wall are obviously linked to the device migration, the role of intravascular blood flow features is still unclear. In this study we analyze the in-stent hemodynamics in a cohort of 20 image-based computational fluid dynamics (CFD) models of EVAR patients, treated with two different commercial endograft devices. By exploring the associations between distinguishable intravascular hemodynamic features *vs.* displacement forces, we aim to identify potential targets of endografts design optimization strategies, a fundamental step in the EVAR risk of failure minimization process. In particular, based on fluid mechanics theoretical remarks, here we focus the attention on in-stent helical flow features, which have also been recently suggested to reduce the risk of thrombosis in implanted endografts (Tasso et al., 2018).

The study additionally involves an analysis of hydraulic resistance and power losses, as it is well-established that helical flow affects the energetic properties of conduits (Liu et al., 2016; Van Canneyt et al., 2013; Zovatto and Pedrizzetti, 2018).

2. Material and methods

The study protocol presented was approved by the Institutional Review Board of the University of Ioannina, Ioannina, Greece, and all subjects gave informed consent for the use of their screening data. Twenty male subjects affected by infrarenal fusiform AAA and treated with EVAR were selected and divided into two equal, statistically homogeneous subgroups, as detailed in the Supplementary Material and elsewhere (Raptis et al., 2017; Tasso et al., 2018): one group was treated with the Endurant (Medtronic Vascular, Santa Rosa, CA) stent graft, the other group was treated with the Excluder (W.L. Gore & Associates, Flagstaff, AZ) stent graft. One month after device implantation, all subjects underwent computed tomography angiography (CTA) and CTA images were segmented using a semi-automatic approach. Image segmentation of the stent-graft internal surface of EVAR treated arteries was carried out. Segmented images were converted into three-dimensional geometries using the commercial code MIMICS (Materialise, Leuven, Belgium). CTA acquisition and geometry reconstruction strategies have been exhaustively described elsewhere (Tasso et al., 2018). The twenty reconstructed geometries are presented in Fig. 1.

The finite volume-based general purpose CFD code FLUENT (ANSYS Inc., Canonsburg, PA) was used to solve the unsteady-state governing equations of motion on fluid domains discretized by tetrahedrons (Tasso et al., 2018). Exhaustive details on the implemented meshing strategy and the applied numerical schemes are reported elsewhere (Tasso et al., 2018), and are summarized in the Supplementary material. Here, blood was assumed to be an incompressible, homogeneous, Newtonian fluid (Iasiello et al., 2017; Tasso et al., 2018). The strategy to prescribe boundary conditions was dictated by the lack of patient-specific hemodynamic data, as already described elsewhere (Tasso et al., 2018). Consequently, the conditions applied at the boundaries were extracted from literature. In detail: (1) at the inlet, the same pressure waveform (Olufsen et al., 2000) was applied to all subjects; (2) at the outflow sections, a time-dependent fully-developed velocity profile was imposed after scaling a flow rate waveform available in the literature (Olufsen et al., 2000) according to the area of each outflow section; (3) the no-slip condition was applied at the wall, following the rigid wall assumption that is commonly made in the context of CFD modeling.

Displacement forces (**DF**s) exerted on the implanted stent graft are given by the summation of two contributions: the body force (the weight force, due to gravity), and the surface forces, due to hemodynamics. In detail, the surface forces are composed by (Fig. 2): the normal component on the endograft surface due to blood pressure, and the tangent component that is the shear force acting on the endograft surface due to blood flow. Here we are interested only on hemodynamic forces acting on the stent graft as possible cause of migration, hence the presence of the gravity was neglected. At a generic time instant t along the cardiac cycle, the net **DF**, applied to the center of mass (CM) of a body of surface area S_i, can be calculated as follows (Kandail et al., 2014):

$$\mathbf{DF}(t) = \int_{S_i} p(\boldsymbol{s},t)\mathbf{n}(\boldsymbol{s})dS + \int_{S_i} \boldsymbol{\tau}_w(\boldsymbol{s},t)dS \tag{1}$$

where p is the pressure, $\mathbf{n}$ is the unit vector normal to the elemental surface of area dS around the generic position $\boldsymbol{s}$, and $\boldsymbol{\tau}_w$ is the wall shear stress vector. Here, **DF** was calculated by integration over different surface areas S_i, in order to obtain the net **DF** acting on the whole reconstructed endograft model, and on each one of the three surface areas obtained by splitting the model into body and legs, according to Fig. 1. Furthermore, according to the method proposed elsewhere (Morbiducci et al., 2015), the net **DF** acting on the body and legs of the implanted stent grafts were projected: along the main blood flow direction, corresponding to the local axial (centerline) direction ($\mathbf{DF}_{//}$); along the direction orthogonal to the axial one ($\mathbf{DF}_{\perp}$).

As net **DF**s vary along the cardiac cycle, here their time-average values (**TADF**) was calculated as follows:

$$\mathbf{TADF} = \frac{1}{T_i}\int_{T_i} \mathbf{DF}(\boldsymbol{s}_{CM},t)dt \tag{2}$$

where T_i is a generic time interval corresponding to the cardiac cycle (T_{CYCLE}), the systolic phase (T_{SYS}), and the diastolic (T_{DIA}) phase.

The performance of the implanted stent grafts was also evaluated in terms of energetics. To do that, the instantaneous hydraulic power losses ($\dot{E}$) was calculated according to the following equation, as proposed elsewhere (Grigioni et al., 2006):

$$\begin{aligned}\dot{E}(t) = &-\int_{IN} p(\boldsymbol{s},t)\boldsymbol{v}(\boldsymbol{s},t)\cdot\mathbf{n}(\boldsymbol{s})dS - \int_{IN}\frac{1}{2}\rho|\boldsymbol{v}(\boldsymbol{s},t)|^2\boldsymbol{v}(\boldsymbol{s},t)\\ &\cdot\mathbf{n}(\boldsymbol{s})dS - \int_{IN} p(\boldsymbol{s},t)\boldsymbol{v}(\boldsymbol{s},t)\cdot\mathbf{n}(\boldsymbol{s})dS - \int_{OUT}\\ &\times\frac{1}{2}\rho|\boldsymbol{v}(\boldsymbol{s},t)|^2\boldsymbol{v}(\boldsymbol{s},t)\cdot\mathbf{n}(\boldsymbol{s})dS\end{aligned} \tag{3}$$

where p is the static pressure, ρ the fluid density, $\boldsymbol{v}$ the velocity vector, and $\mathbf{n}$ is the unit vector normal to the generic elemental surface of area dS of the inflow (IN) and outflow (OUT) sections of the stent graft, pointing outward. As an additional descriptor of the stent graft performance, the pressure drop ($\Delta p(t)$) between the inlet and outlet sections was used to evaluate the average resistance of the implanted stent grafts to flow:

$$R = \frac{\mathrm{TA}\Delta p}{Q_{avg}} \tag{4}$$

where $\mathrm{TA}\Delta p$ and Q_{avg} are the cycle-average values of Δp and of the flow rate at the inflow section of each model, respectively. Here Δp was evaluated as the mean value of the pressure drop between the inlet section of the device and each one of the two outlet sections.

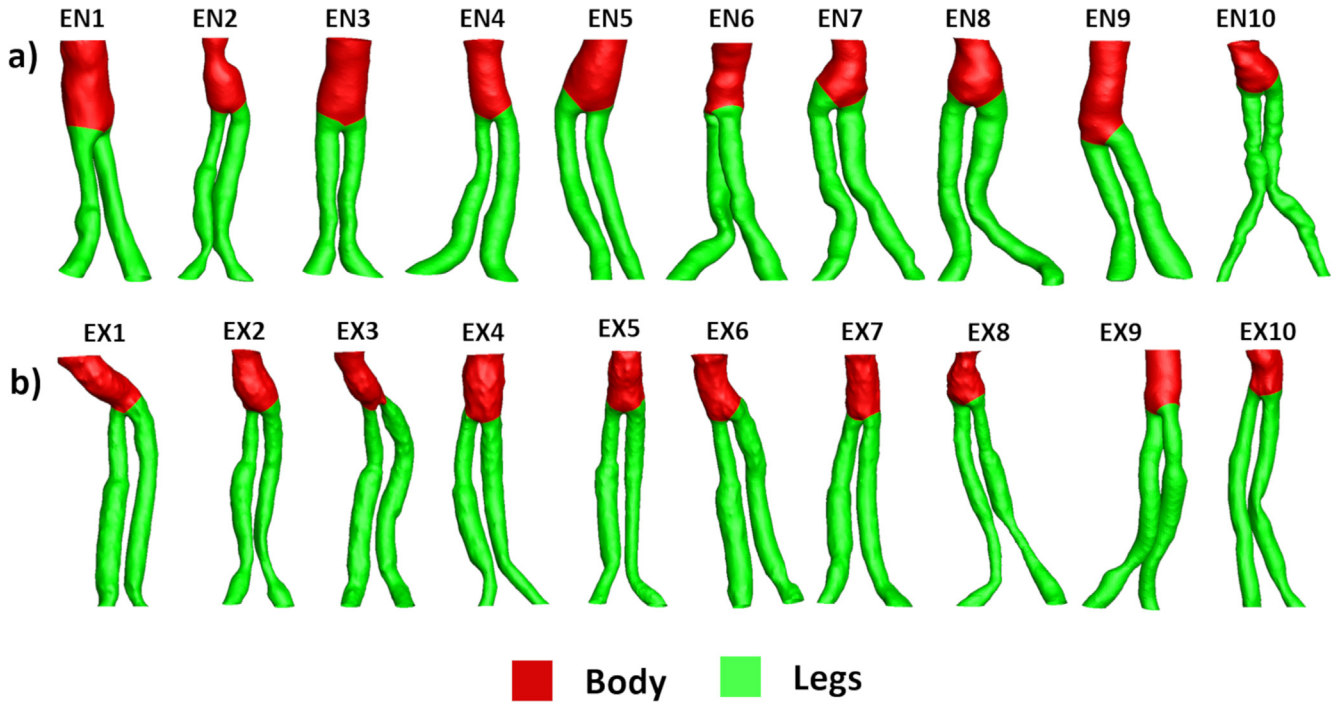

Fig. 1. Models of the 20 investigated EVAR-treated subjects: (a) graft geometries of patients treated with Endurant; (b) graft geometries of patients treated with Excluder. For each model, the body (the segment upstream of the bifurcation, red colour) and legs (segments downstream of the bifurcation, green colour) are shown. (For interpretation of the references to colour in this figure legend, the reader is referred to the web version of this article.)

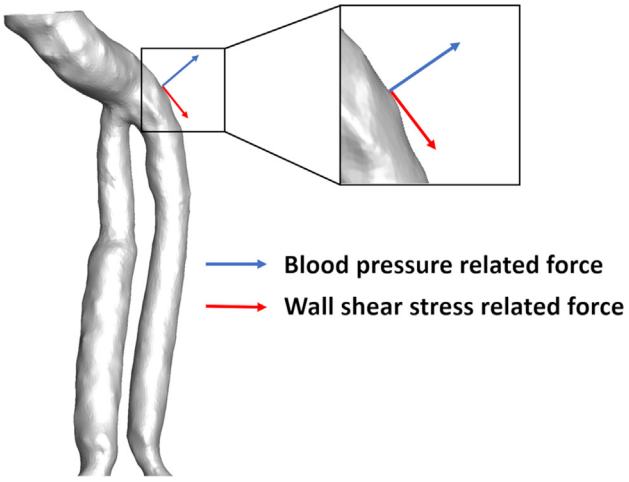

Fig. 2. Explanatory example of the direction of hemodynamic surface forces, i.e., the normal component on the endograft surface due to blood pressure, and the tangent component that is the shear force acting on the endograft surface due to blood flow.

To complete the analysis, fluid structures inside the stent grafts were characterized in terms of helical blood flow, motivated by: (1) the recently observed positive association between wall shear stress (WSS) magnitude and helicity intensity (i.e., the lower the helicity intensity, the lower the WSS and consequently the higher the WSS-related risk of thrombosis, as low WSS is a well-recognized blood flow feature promoting thrombus formation) on the same dataset of stent grafts (Tasso et al., 2018); (2) the fact that helical flow as imparted by geometric features affect the energetic properties of a vessel/conduit (Liu et al., 2016; Van Canneyt et al., 2013; Zovatto and Pedrizzetti, 2018). The helicity-based hemodynamic descriptor defined elsewhere (Gallo et al., 2012; Morbiducci et al., 2013), the time and volume-average helicity intensity (h_2), was evaluated as follows:

$$h_2 = \frac{1}{T_i V_i} \int_{T_i} \int_{V_i} |\boldsymbol{v}(\boldsymbol{s},t) \cdot \boldsymbol{\omega}(\boldsymbol{s},t)| dV dt \tag{5}$$

where V_i are the fluid volumes of the stent graft or of its parts (as displayed in Fig. 1), T_i is the integration interval, $\boldsymbol{v}$ is the velocity vector and $\boldsymbol{\omega}$ is the vorticity vector. The analysis of helical flow structures was enriched considering the helicity topology indicator (h_4):

$$h_4 = \frac{|h_1|}{h_2} \tag{6}$$

where h_1 is the time and volume-average helicity:

$$h_1 = \frac{1}{T_i V_i} \int_{T_i} \int_{V_i} \boldsymbol{v}(\boldsymbol{s},t) \cdot \boldsymbol{\omega}(\boldsymbol{s},t) dV dt \tag{7}$$

As reported elsewhere, h_4 measures the strength of relative rotations of helical fluid structures in the fluid domain (Gallo et al., 2012; Morbiducci et al., 2013). The calculation of all descriptors was implemented in the programming code Python and the open-source software VMTK (Antiga et al., 2008).

Finally, a statistical analysis was carried out. The Mann-Whitney test (Mann et al., 1947) was preliminary applied to verify if there are significant differences between groups treated with different stent graft commercial devices. Over the sample obtained by pooling together the Endurant and the Excluder groups of implanted subjects, the existence of possible one-to-one associations among **DF**s and intra-endograft hemodynamics was explored using the Pearson correlation coefficient in case both variables were normally distributed and using Spearman correlation coefficient if at least one variable was not normally distributed. Statistical significance was assumed for $p < 0.05$. The statistical analyses were performed using MATLAB® (The Math Works, Inc., Natick, MA).

3. Results

In terms of geometry, Endurant and Excluder models presented comparable average values of stent graft surface area ($0.0112 \pm 0.0018\ m^2$ and $0.0096 \pm 0.0008\ m^2$, respectively) and cross-sectional inlet area ($3.30 \cdot 10^{-4} \pm 1.23 \cdot 10^{-4}\ m^2$ and $2.32 \cdot 10^{-4} \pm 0.48 \cdot 10^{-4}\ m^2$, respectively), as confirmed by a Mann-Whitney test ($p > 0.05$).

The magnitude of resultant **DF**s along the cardiac cycle are reported in Fig. 3. **DF**s were always higher in subjects treated with the Endurant stent graft (Fig. 3; individual **DF** magnitude time histories are presented in Fig. S1 of the Supplementary material). This observation was confirmed by group-averaged **TADF** and **DF** peak magnitude ($\mathbf{DF}_{peak}$) values (Fig. 4; individual **DF** peak magnitude values are presented in Fig. S2 of the Supplementary material). Overall, the observed **DF** values are below 7.1 N. Interestingly, a statistically significant difference in **TADF** (averaged along the whole cardiac cycle, systole and diastole) and **DF** peak magnitude was observed between the two devices only in the legs ($p < 0.01$, Fig. 4). **DF** average magnitude and peak data are summarized in Tables S1 (whole stent graft), S2 (body) and S3 (legs) of the Supplementary material.

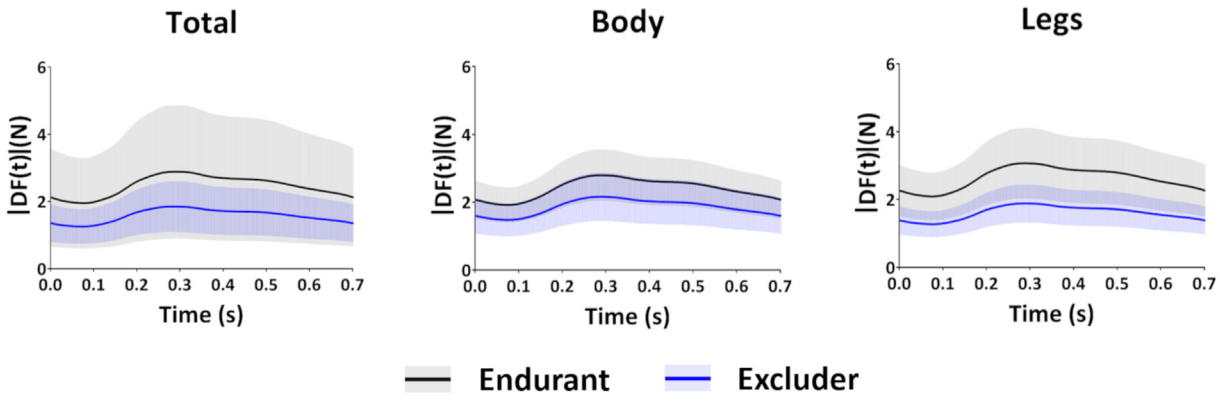

Fig. 3. Group-averaged instantaneous **DF**s magnitude values along the cardiac cycle in Endurant (black line) and Excluder (blue line) models. Shaded areas highlight ± one standard deviation range. (For interpretation of the references to colour in this figure legend, the reader is referred to the web version of this article.)

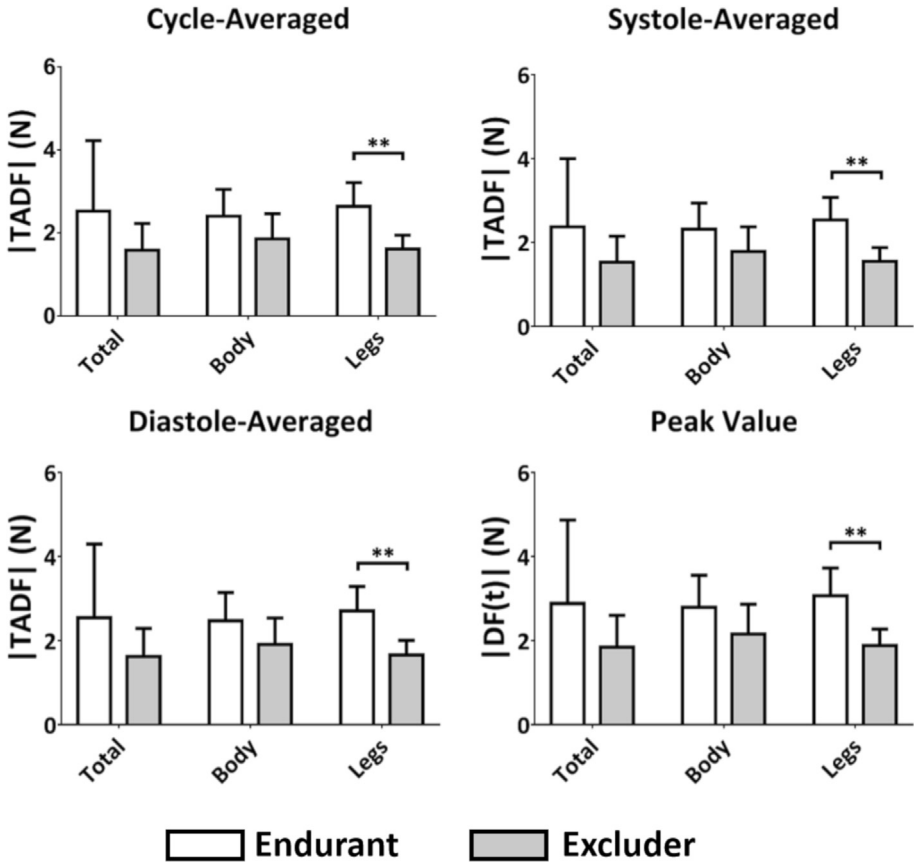

Fig. 4. TADF magnitude (averaged over the whole cardiac cycle, systole and diastole) and $\mathbf{DF}_{peak}$ magnitude values for the two analysed groups of EVAR-treated patients (Endurant and Excluder) in the three regions of interest (total, body and legs). Statistically significant difference is indicated with ** ($p < 0.01$).

To complete the analysis, stent graft body and single leg time-average resultant **TADF** vectors and their point of application are shown, for all patients, in Fig. 5. It can be observed that **TADF** vectors present a heterogeneous orientation, with respect to the local axial direction (Fig. 5). This observation stimulated a more detailed analysis in the body and in the legs, splitting **DF**s into the two constituent components along the main (axial) blood flow direction and along the direction orthogonal to the axial one. The results reported in Fig. 6 show that, on average: (1) in the body, subjects treated with the Excluder undergo $\mathbf{TADF}_{\perp}$ magnitude values twice the value of $\mathbf{TADF}_{//}$, while the magnitude of the two **DF** components is almost the same in subjects treated with the Endurant; (2) in the legs, $\mathbf{TADF}_{\perp}$ magnitude values are around three times and more than two times $\mathbf{TADF}_{//}$ magnitude in subjects treated with the Excluder and Endurant, respectively. The same ratios between the two constituent components were observed for the **DF** peak magnitude. Significant differences between the two groups of subjects were observed only in cycle-average and peak magnitude of the **DF** component orthogonal to the stent graft axis ($p < 0.01$; see also Tables S2 and S3 of Supplementary material).

The stent performance was then evaluated using TAΔp and R values. Both were significantly lower in subjects treated with the Endurant ($p < 0.01$, Fig. 7). Not significant difference was observed

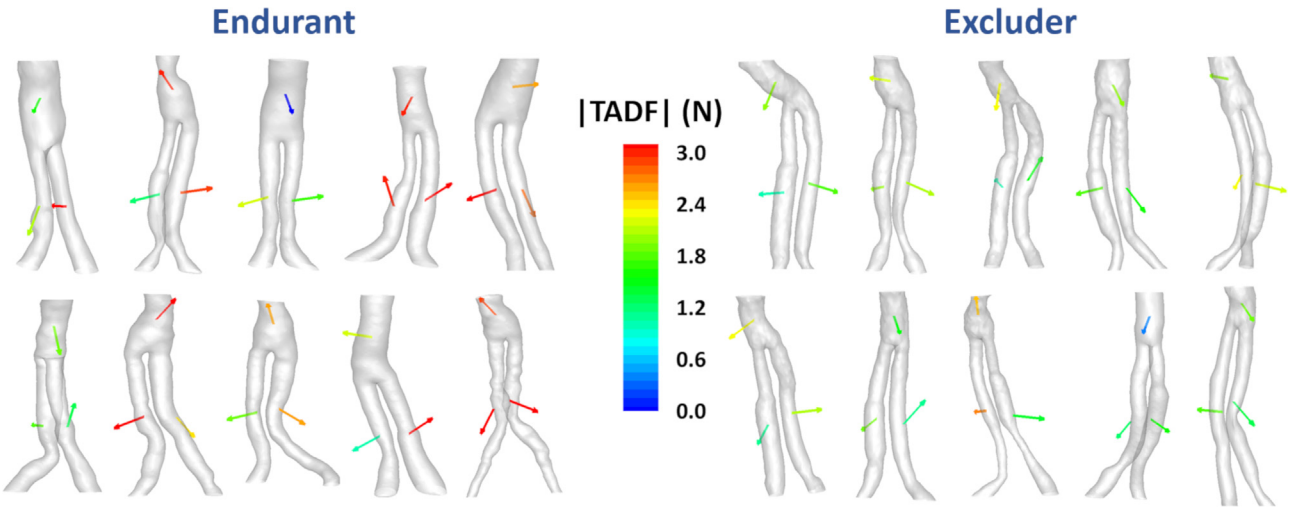

Fig. 5. Cycle-averaged **DF** (non-scaled length) vectors applied in the centre of mass of body and legs for the two analysed groups of EVAR-treated patients (Endurant and Excluder). Vectors magnitude is represented by the colour map.

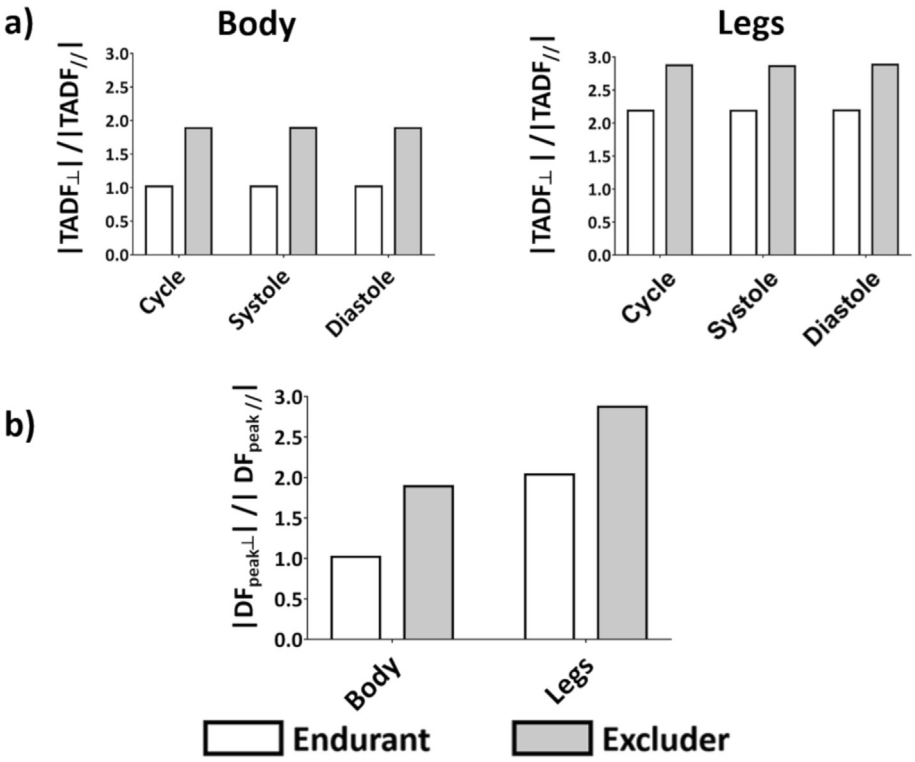

Fig. 6. Group-averaged (a) $\mathbf{TADF}_{\perp}$ over $\mathbf{TADF}_{//}$ magnitude values, and (b) $\mathbf{DF}_{peak\perp}$ over $\mathbf{DF}_{peak//}$ magnitude values.

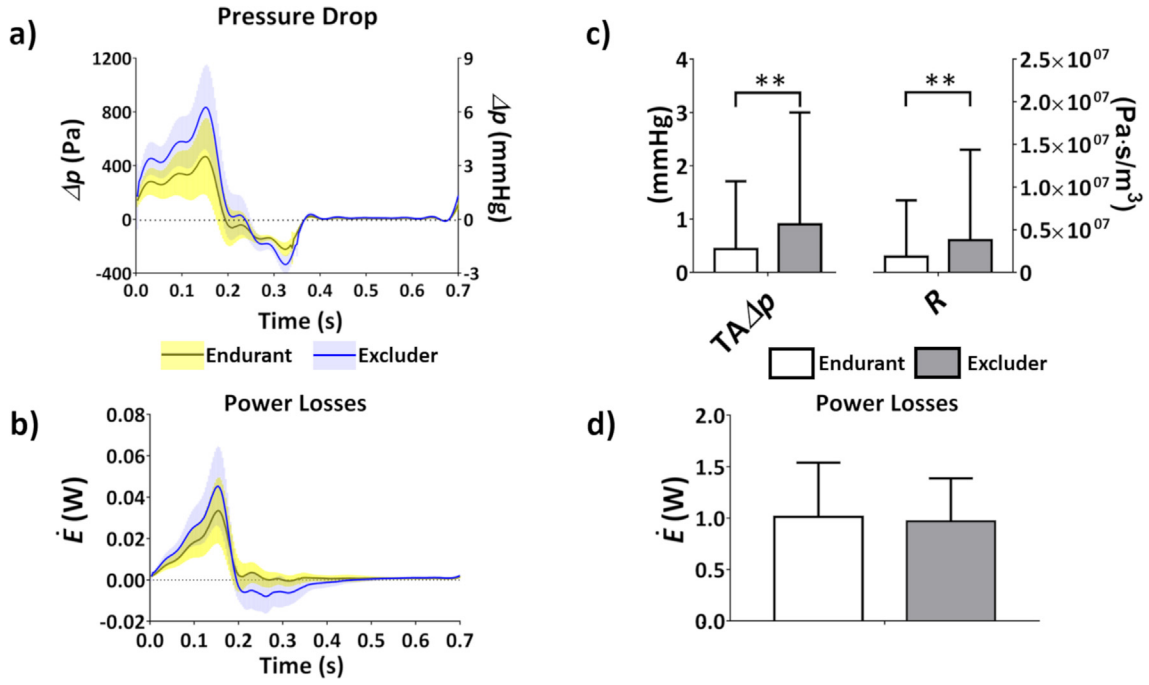

Fig. 7. Group-averaged (shaded areas indicate ± one standard deviation range) instantaneous: pressure drop (a) and power losses (b) values along the cardiac cycle. Group-averaged pressure drop and hydraulic resistance values averaged over the cardiac cycle (TAΔp and R, respectively) are presented in panel (c), while total power loss values ($\dot{E}$) are presented in panel (d). Statistically significant differences are indicated with ** ($p < 0.01$).

in cycle-average power losses values between Endurant and Excluder.

Concerning helical flow characterization, results in Fig. 8 confirm previous observations of higher helicity intensity in Excluder group, for each temporal integration interval considered (Fig. 8, left panel). Widening the analysis to stent grafts body and legs, significant differences in helicity intensity were observed between Endurant and Excluder groups in the legs of the endografts. Overall, the low values observed for h_4 (Fig. 8, right panel) suggest the presence of balanced counter-rotating helical structures in the body and in the legs of the endografts.

The interaction between intravascular hemodynamics and displacement forces was then investigated. The explanatory example in Fig. 9 presents, in the two Endurant models characterized by the extreme values of peak **DF** magnitude, instantaneous helical flow features in terms of isosurfaces of LNH (Local Normalized Helicity, $-1 \leq \mathrm{LNH} \leq 1$), i.e., the normalized internal product of $\boldsymbol{v}$ and $\boldsymbol{\omega}$ vectors (Morbiducci et al., 2007). Adopting high threshold values of LNH for the visualization of blood flow structures, it was possible to observe that the stent graft model characterized by the lowest peak **DF** magnitude value presented a more marked helical flow content.

The statistical analysis confirmed that, considering the whole stent graft model, a moderate negative association emerged between **TADF** magnitude and h_2 for every integration interval (Table 1). A more detailed analysis was carried out in the stent graft body and legs separately. In detail (Table 1): (1) in the body, h_2 was found to be positively associated to **TADF** magnitude in diastole ($p < 0.04$) and to the cycle-average $\mathbf{TADF}_{//}$ magnitude ($p < 0.02$); (2) in the legs, cycle- and systole-average **TADF** and $\mathbf{TADF}_{\perp}$ magnitude values were found to be inversely associated to cycle-average ($p < 0.02$ and, $p < 0.04$, respectively) and to systole-average ($p < 0.0007$ and $p < 0.02$, respectively) h_4 values, while an inverse association emerged between h_2 and diastole-average **TADF** and $\mathbf{TADF}_{\perp}$ magnitude values ($p < 0.02$ and $p < 0.05$, respectively).

Considering the energetic descriptors, the statistical analysis reported in Table 2 highlighted a positive association of h_2 with Δp and R over the whole cardiac cycle and over systole. Over diastole, helical flow intensity was inversely associated to the power losses (Table 2).

4. Discussion

Previous findings identify ill directional **DF**s exerted on stent grafts as biomechanical triggers of adverse events in patients undergoing EVAR, with the induced stent graft migration to determine hostile postoperative scenarios that could lead to the ultimate failure of the device (Kandail et al., 2014). The possibility that the hemodynamic forces acting on the stent graft correlate with the risk of device failure, has stimulated the research towards the quantification of the hemodynamic environment inside post-EVAR models through image-based CFD simulations (Figueroa et al., 2009; Kandail et al., 2014; Molony et al., 2010; Stefanov et al., 2013). In this perspective, the present study is motivated by the need for a more robust assessment of the hemodynamic-triggered risk of post-EVAR adverse events. Based on recent computational findings highlighting that the clinically observed propensity to thrombus formation in EVAR-devices could be explained in terms of distinguishable in-stent helical flow features (Raptis et al., 2016; Raptis et al., 2017), here we widen the analysis to explore the existence of possible links among stent graft displacement forces, helical flow, pressure drops, and hydraulic power losses in a dataset of 20 patients treated with two different commercial endovascular grafts.

The analysis highlighted that in general **TADF** and peak **DF** magnitudes were always higher in the Endurant group, but significant differences were observed only in the legs (Fig. 4). Separating the displacement forces in two projections, i.e. along the axis of the implanted stent graft and orthogonal to it, a statistical difference between the two groups was observed only for $\mathbf{TADF}_{\perp}$ and peak $\mathbf{DF}_{\perp}$ magnitude in the legs (Table S3).

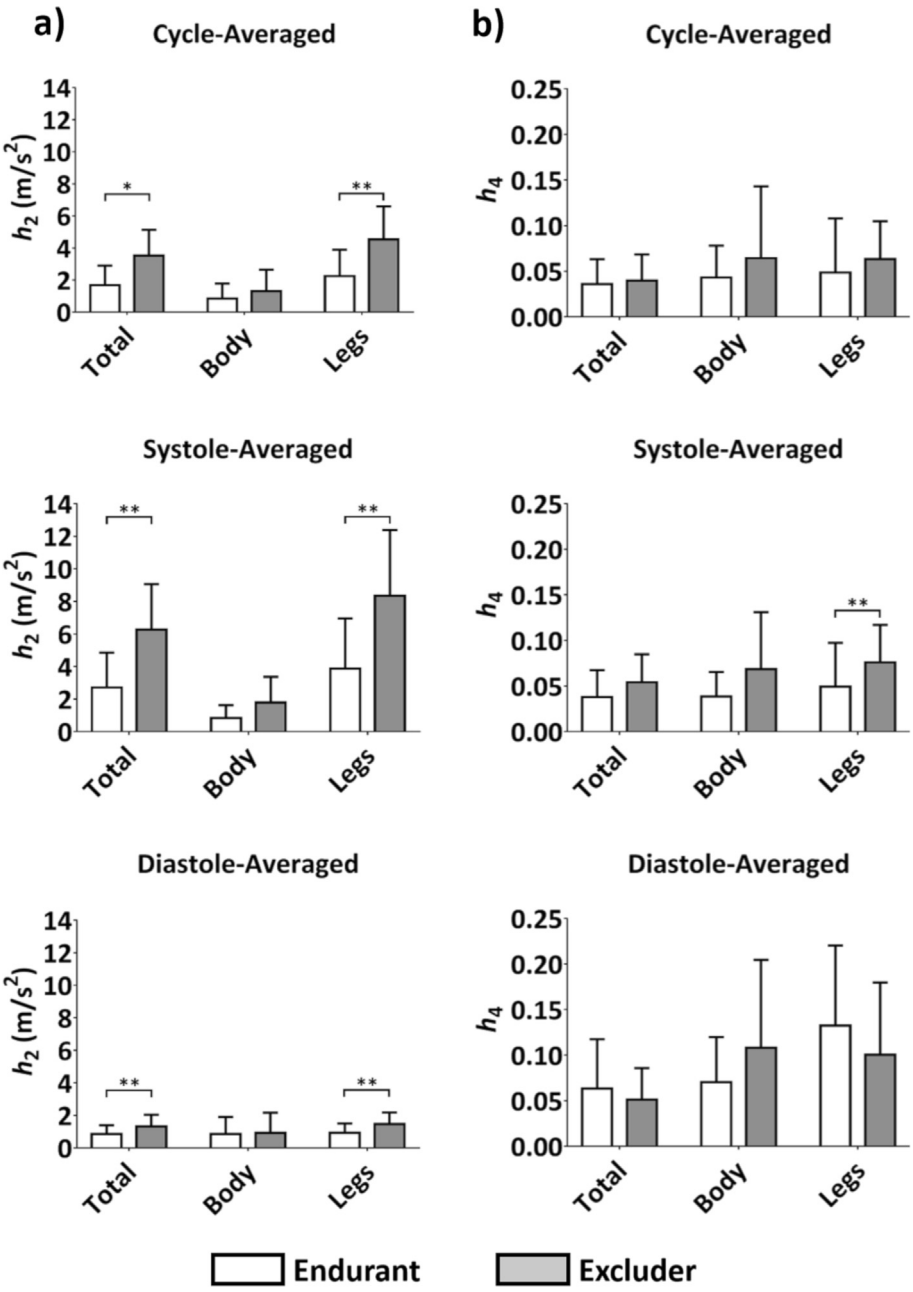

Fig. 8. Group-averaged helicity intensity h_2 (a) and helicity topology indicator h_4 (b) values, averaged over cardiac cycle, systole and diastole. Data are reported for the three regions of interest (total, body and legs) of the device. Statistically significant differences are indicated with * ($p < 0.05$) and ** ($p < 0.01$).

Interestingly, features common to both groups emerged (Fig. 6): (1) **TADF**$_\perp$ magnitude was at least twice the value of **TADF**$_{//}$ in the legs area; (2) for peak displacement forces, **DF**$_\perp$ magnitude was similar to **DF**$_{//}$ in the body, but at least the double of the value in the legs. These findings warrant further investigation with follow-up studies on patients undergoing EVAR, aiming at clarifying if endograft migration is mainly ascribable to the action of a displacement force components acting along the axis of the implanted device or normal to it. From such follow up studies, applying the same strategy as the one proposed here, clear indications could emerge for the design optimization of EVAR stent grafts.

Overall, significantly lower pressure drops were observed in the Endurant group, while similar levels of power losses were observed in the two groups (Fig. 7). Helicity intensity was observed to be higher in the Excluder group for all cases, and differences between the two groups are significant, except for the body (Fig. 8). The comparison between the two groups highlights that, overall, pressure drops, and helicity intensity are higher in the Excluder group, where displacement forces are lower.

To search for emerging features, the associations among intra-stent hemodynamic features, displacement forces, resistance to flow and hydraulic power losses were tested in the population obtained by pooling together Endurant and Excluder groups. From the analysis considering the whole stent graft, an inverse association between **TADF** and h_2 emerged (i.e., the higher the helicity intensity inside the stent graft, the lower the displacement forces acting on the graft walls) (Table 1). This result becomes particularly relevant combined with findings from a previous study on the same dataset (Tasso et al.,

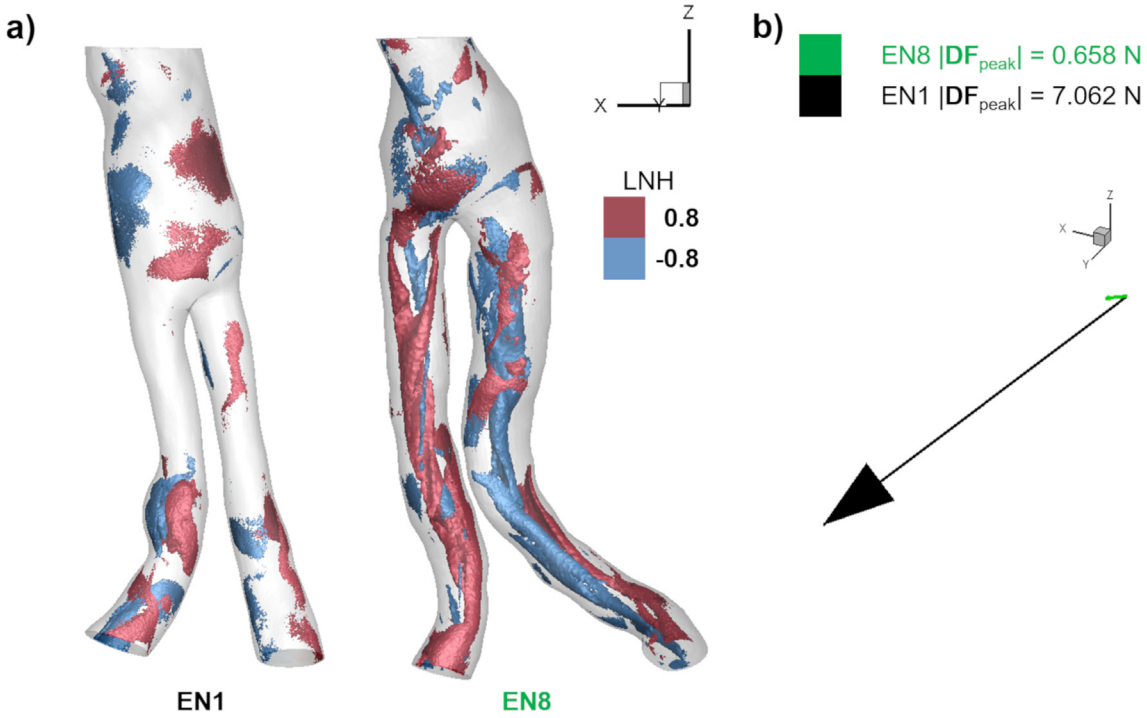

Fig. 9. Visualization of intravascular LNH isosurfaces (a) and **DF** vectors (b) at peak systole for the two selected patients presenting the highest (EN1) and the lowest (EN8) $\mathbf{DF}_{peak}$ magnitude values (both patients were treated with Endurant). Right-handed helical structures are associated with positive LNH values (red colour) and left-handed helical structures are associated with negative LNH values (blue colour). $\mathbf{DF}_{peak}$ vectors arrows are scaled according to values of $\mathbf{DF}_{peak}$ magnitude. The different orientation of reference frame is to better appreciate both helical flow structures and $\mathbf{DF}_{peak}$ vectors magnitude and direction. (For interpretation of the references to colour in this figure legend, the reader is referred to the web version of this article.)

Table 1
Correlation (in terms of correlation coefficient) between helical flow descriptors and time averaged displacement forces magnitude. *indicates $p < 0.05$ and **indicates $p < 0.01$.

	h_2	h_4	h_2	h_4	h_2	h_4
	Cycle Averaged		Systole Averaged		Diastole Averaged	
			Total			
|TADF|	−0.4677*	−0.2015	−0.4827*	−0.3128	−0.5006*	0.3353
			Body			
|TADF|	0.4090	−0.1579	0.1835	0.8313	0.4767*	−0.1444
$\mathbf{\|TADF_{//}\|}$	0.5233*	−0.0150	0.4045	0.0707	0.4045	0.0707
$\mathbf{\|TADF_{\perp}\|}$	−0.2737	−0.1654	−0.2481	−0.2256	−0.2481	−0.2256
			Legs			
|TADF|	−0.2701	−0.3824*	−0.2664	−0.5212**	−0.3568*	0.1424
$\|TADF_{//}\|$	0.0779	−0.0929	0.0675	−0.2336	−0.0835	−0.1235
$\|TADF_{\perp}\|$	−0.2062	−0.3285*	−0.2049	−0.3749*	−0.3133*	0.2349

Table 2
Correlation (in terms of correlation coefficient) between helical flow descriptors and energetic descriptors (power losses, hydraulic resistance and pressure drop). * indicates $p < 0.05$, ǂindicates $p < 0.001$.

	h_2	h_4	h_2	h_4	h_2	h_4
	Cycle Averaged		Systole Averaged		Diastole Averaged	
$\dot{E}$	0.0707	−0.2436	0.3774	0.0030	−0.5188*	0.1399
R	0.9083ǂ	0.1220	0.9015ǂ	0.3019	0.5777ǂ	−0.1471
Δp	0.9197ǂ	0.1452	0.9219ǂ	0.2865	−0.664	−0.0278

2018), reporting of a beneficial role of helical flow intensity in suppressing low velocity/stagnation regions (Gallo et al., 2012; Morbiducci et al., 2010), that are well-recognized blood flow features promoting thrombus formation. The analysis highlighted also: (1) an inverse association of h_4 to **TADF** and $\mathbf{TADF}_{\perp}$ magnitude in the legs, suggesting that in that part of the endograft the more unbalanced are the counter-rotating helical flow structures (corresponding to high h_4 value), the smaller the displacement forces; (2) the association between helical flow and displacement forces in the body is positive, in opposition to what observed considering the whole device, suggesting that there is room for improving the hemodynamics in this part of the device, optimizing its design for the establishment of beneficial helical flow structures.

In terms of energetics, overall helical flow intensity is positively associated to pressure drop and resistance to flow, as expected (Table 2). However, such increase in pressure drop is here clinically irrelevant. On the other hand, the beneficial, inverse association between helical flow intensity and power losses in diastole can be explained considering the already mentioned ability of helical flow structures in reducing flow reversal (Gallo et al., 2018; Gallo et al., 2012; Morbiducci et al., 2010; Morbiducci et al., 2016; Morbiducci et al., 2010; Tasso et al., 2018).

There are some limitations that could weaken the findings of this study and that should be discussed here. One main limitation, as acknowledged elsewhere (Raptis et al., 2017; Tasso et al., 2018), is that it was not possible to apply personalized boundary conditions, since patient-specific hemodynamic data were not available. However, when considering displacement forces, the reported scarce sensitivity to moderate variations at inflow boundaries (Figueroa et al., 2010) mitigates the uncertainty introduced in our findings by applying literature-derived boundary conditions. Moreover, it has been already observed that the complex upstream aortic flow patterns, here not included in the model, do not markedly impact the in-stent hemodynamics and displacement forces, in particular in the distal legs (Stefanov et al., 2013). More attention should be reserved in interpreting the results here obtained in the body of the device, which is more sensitive to the complexity of the hemodynamics in the proximal aorta (Stefanov et al., 2013). Moreover, as the model reconstruction was limited to the stent graft internal surface assumed as rigid, it is not possible to ascertain the role of neck angulation (Kandail et al., 2014) or of the mismatch between the mechanical properties between the aortic wall and the stent-graft (Morris et al., 2016) in the establishment of helical flow patterns. In addition, it should be underlined that in this study the **DFs** were computed at rest condition; in case of hypertension or exercise conditions the magnitude of **DFs** would be considerably higher (Kandail et al., 2016). Finally, it should be highlighted that a higher sample size would enforce the obtained results.

To conclude, the findings of this study suggest that: (1) distinguishable helical flow features inside the implanted endovascular device, being inversely associated to the risk of stent graft migration as well as to the risk of thrombus apposition (Tasso et al., 2018), could be the ideal candidate in a device design optimization perspective, and deserves further investigation; (2) the observed beneficial role of increased helical content of the in-stent hemodynamics could be partially limited by the fact that a higher helicity intensity implies increased flow resistance. However, per point 2, it should be noticed that pressure drops affecting the performance of the implanted endografts object of this study are clinically irrelevant.

In conclusion, this study suggests a helical flow-driven design strategy applied to EVAR devices to minimize the clinical risk, because an enhanced in-stent graft helical flow content could not only reduce the risk of thrombosis (Tasso et al., 2018), but also the displacement forces acting on the device, an hallmark of increased risk of migration events.

Declaration of Competing Interest

The authors have no professional or financial conflicts of interest to disclose.

Appendix A. Supplementary material

Supplementary data to this article can be found online at https://doi.org/10.1016/j.jbiomech.2019.07.034.

References

Ailawadi, G., Eliason, J.L., Upchurch, G.R., 2003. Current concepts in the pathogenesis of abdominal aortic aneurysm. J. Vasc. Surg. 38 (3), 584–588.

Antiga, L., Piccinelli, M., Botti, L., Ene-Iordache, B., Remuzzi, A., Steinman, D.A., 2008. An image-based modeling framework for patient-specific computational hemodynamics. Med. Biol. Eng. Compu. 46 (11), 1097–1112.

Bastos, G.F., Rouwet, E.V., Metz, R., Hendriks, J., Muhs, B., Verhagen, H., 2010. Device-specific outcomes after endovascular abdominal aortic aneurysm repair. J. Cardiovasc. Surg. 51 (4), 515–531.

Budtz-Lilly, J., Venermo, M., Debus, S., Behrendt, C.A., Altreuther, M., Beiles, B., Szeberin, Z., Eldrup, N., Danielsson, G., Thomson, I., Wigger, P., Björck, M., Loftus, I., Mani, K., 2017. Editor's choice – assessment of international outcomes of intact abdominal aortic aneurysm repair over 9 years. Eur. J. Vasc. Endovasc. Surg. 54 (1), 13–20.

Chang, R.W., Goodney, P., Tucker, L.-Y., Okuhn, S., Hua, H., Rhoades, A., Sivamurthy, N., Hill, B., 2013. Ten-year results of endovascular abdominal aortic aneurysm repair from a large multicenter registry. J. Vasc. Surg. 58 (2), 324–332.

Daye, D., Walker, T.G., 2018. Complications of endovascular aneurysm repair of the thoracic and abdominal aorta: evaluation and management. Cardiovasc. Diagn. Ther. 8 (S1), S138–S156.

Desai, M., Eaton-Evans, J., Hillery, C., Bakhshi, R., You, Z., Lu, J., Hamilton, G., Seifalian, A.M., 2010. AAA stent-grafts: past problems and future prospects. Ann. Biomed. Eng. 38 (4), 1259–1275.

Figueroa, C.A., Taylor, C.A., Yeh, V., Chiou, A.J., Gorrepati, M.L., Zarins, C.K., 2010. Preliminary 3D computational analysis of the relationship between aortic displacement force and direction of endograft movement. J. Vasc. Surg. 51 (6), 1488–1497.

Figueroa, C.A., Taylor, C.A., Yeh, V., Chiou, A.J., Zaris, C.K., 2009. Effect of curvature on displacement forces acting on aortic endografts: A 3-dimensional computational analysis. J. Endovasc. Ther. 16, 284–294.

Gallo, D., Bijari, P.B., Morbiducci, U., Qiao, Y., Xie, Y., Etesami, M., Habets, D., Lakatta, E.G., Wasserman, B.A., Steinman, D.A., 2018. Segment-specific associations between local haemodynamic and imaging markers of early atherosclerosis at the carotid artery: an *in vivo* human study. J. R. Soc. Interface 15 (147).

Gallo, D., Steinman, D.A., Bijari, P.B., Morbiducci, U., 2012. Helical flow in carotid bifurcation as surrogate marker of exposure to disturbed shear. J. Biomech. 45 (14), 2398–2404.

Grigioni, M., D'Avenio, G., Amodeo, A., Di Donato, R.M., 2006. Power dissipation associated with surgical operations' hemodynamics: Critical issues and application to the total cavopulmonary connection. J. Biomech. 39 (9), 1583–1594.

Iasiello, M., Vafai, K., Andreozzi, A., Bianco, N., 2017. Analysis of non-Newtonian effects within an aorta-iliac bifurcation region. J. Biomech. 64, 153–163.

Kandail, H., Hamady, M., Xu, X.Y., 2014. Patient-specific analysis of displacement forces acting on fenestrated stent grafts for endovascular aneurysm repair. J. Biomech. 47 (14), 3546–3554.

Kandail, H.S., Hamady, M., Xu, X.Y., 2016. Hemodynamic functions of fenestrated stent graft under resting, hypertension, and exercise conditions. Front. Surg. 3.

Kent, F., Ambler, G.K., Bosanquet, D.C., Twine, C.P., Bell, R., Bicknell, C.D., Coughlin, P.A., Hayes, P.D., Jenkins, M., Lewis, D., Vallabhaneni, R., Zayed, H., 2018. The safety of device registries for endovascular abdominal aortic aneurysm repair: systematic review and meta-regression. Eur. J. Vasc. Endovasc. Surg. 55 (2), 177–183.

Kontopodis, N., Antoniou, S.A., Georgakarakos, E., Ioannou, C.V., 2015. Endovascular vs open aneurysm repair in the young. J. Endovasc. Ther. 22 (6), 897–904.

Liu, X., Wang, L., Wang, Z., Li, Z., Kang, H., Fan, Y., Sun, A., Deng, X., 2016. Bioinspired helical graft with taper to enhance helical flow. J. Biomech. 49 (15), 3643–3650.

Mann, H.B., Whitney, D.R., 1947. On a test of whether one of two random variables is stochastically larger than the other. Ann. Math. Stat. 18 (1), 50–60.

Mohan, I.V., Harris, P.L., van Marewijk, C.J., Laheij, R.J., How, T.V., 2002. Factors and forces influencing stent-graft migration after endovascular aortic aneurysm repair. J. Endovasc. Ther. 9 (6), 748.

Molony, D.S., Kavanagh, E.G., Madhavan, P., Walsh, M.T., McGloughlin, T.M., 2010. A computational study of the magnitude and direction of migration forces in patient-specific abdominal aortic aneurysm stent-grafts. Eur. J. Vasc. Endovasc. Surg. 40 (3), 332–339.

Morbiducci, U., Gallo, D., Cristofanelli, S., Ponzini, R., Deriu, M.A., Rizzo, G., Steinman, D.A., 2015. A rational approach to defining principal axes of multidirectional wall shear stress in realistic vascular geometries, with application to the study of the influence of helical flow on wall shear stress directionality in aorta. J. Biomech. 48 (6), 899–906.

Morbiducci, U., Gallo, D., Ponzini, R., Massai, D., Antiga, L., Montevecchi, F.M., Redaelli, A., 2010a. Quantitative analysis of bulk flow in image-based hemodynamic models of the carotid bifurcation: the influence of outflow conditions as test case. Ann. Biomed. Eng. 38 (12), 3688–3705.

Morbiducci, U., Kok, A.M., Kwak, B.R., Stone, P.H., Steinman, D.A., Wentzel, J.J., 2016. Atherosclerosis at arterial bifurcations: evidence for the role of haemodynamics and geometry. Thromb. Haemost. 115 (3), 484–492.

Morbiducci, U., Ponzini, R., Gallo, D., Bignardi, C., Rizzo, G., 2013. Inflow boundary conditions for image-based computational hemodynamics: Impact of idealized versus measured velocity profiles in the human aorta. J. Biomech. 46 (1), 102–109.

Morbiducci, U., Ponzini, R., Grigioni, M., Redaelli, A., 2007. Helical flow as fluid dynamic signature for atherogenesis risk in aortocoronary bypass. A numeric study. J. Biomech. 40 (3), 519–534.

Morbiducci, U., Ponzini, R., Rizzo, G., Cadioli, M., Esposito, A., Montevecchi, F.M., Redaelli, A., 2010b. Mechanistic insight into the physiological relevance of helical blood flow in the human aorta: an in vivo study. Biomech. Model. Mechanobiol. 10 (3), 339–355.

Morris, L., Stefanov, F., Hynes, N., Diethrich, E.B., Sultan, S., 2016. An experimental evaluation of device/arterial wall compliance mismatch for four stent-graft devices and a multi-layer flow modulator device for the treatment of abdominal aortic aneurysms. Eur. J. Vasc. Endovasc. Surg. 51 (1), 44–55.

Olufsen, M.S., Peskin, C.S., Kim, W.Y., Pedersen, E.M., Nadim, A., Larsen, J., 2000. Numerical simulation and experimental validation of blood flow in arteries with structured-tree outflow conditions. Ann. Biomed. Eng. 28, 1281–1299.

Powell, J.T., Sweeting, M.J., Ulug, P., Blankensteijn, J.D., Lederle, F.A., Becquemin, J.P., Greenhalgh, R.M., 2017. Meta-analysis of individual-patient data from EVAR-1, DREAM, OVER and ACE trials comparing outcomes of endovascular or open repair for abdominal aortic aneurysm over 5 years. Br. J. Surg. 104 (3), 166–178.

Raptis, A., Xenos, M., Georgakarakos, E., Kouvelos, G., Giannoukas, A., Labropoulos, N., Matsagkas, M., 2016. Comparison of physiological and post-endovascular aneurysm repair infrarenal blood flow. Comput. Methods Biomech. Biomed. Eng. 20 (3), 242–249.

Raptis, A., Xenos, M., Georgakarakos, E., Kouvelos, G., Giannoukas, A., Matsagkas, M., 2017. Hemodynamic profile of two aortic endografts accounting for their postimplantation position. J. Med. Devices 11, (2) 021003.

Stefanov, F., McGloughlin, T., Delassus, P., Morris, L., 2013. Hemodynamic variations due to spiral blood flow through four patient-specific bifurcated stent graft configurations for the treatment of abdominal aortic aneurysms. Int. J. Numer. Methods Biomed. Eng. 29 (2), 179–196.

Sweeting, M.J., Balm, R., Desgranges, P., Ulug, P., Powell, J.T., 2015. Individual-patient meta-analysis of three randomized trials comparing endovascularversusopen repair for ruptured abdominal aortic aneurysm. Br. J. Surg. 102 (10), 1229–1239.

Tasso, P., Raptis, A., Matsagkas, M., Rizzini, M.L., Gallo, D., Xenos, M., Morbiducci, U., 2018. Abdominal aortic aneurysm endovascular repair: profiling postimplantation morphometry and hemodynamics with image-based computational fluid dynamics. J. Biomech. Eng. 140 (11), 111003–111012.

Turney, E.J., Steenberge, S.P., Lyden, S.P., Eagleton, M.J., Srivastava, S.D., Sarac, T.P., Kelso, R.L., Clair, D.G., 2014. Late graft explants in endovascular aneurysm repair. J. Vasc. Surg. 59 (4), 886–893.

Van Canneyt, K., Morbiducci, U., Eloot, S., De Santis, G., Segers, P., Verdonck, P., 2013. A computational exploration of helical arterio-venous graft designs. J. Biomech. 46 (2), 345–353.

Van Marrewijk, C.J., Leurs, L.J., Vallabhaneni, S.R., Harris, P.L., Buth, J., Laheij, R.J., 2005. Risk-adjusted outcome analysis of endovascular abdominal aortic aneurysm repair in a large population: how do stent-grafts compare? J. Endovasc. Ther.. 12 (4), 417–429.

Winterborn, R.J., Amin, I., Lyratzopoulos, G., Walker, N., Varty, K., Campbell, W.B., 2009. Preferences for endovascular (EVAR) or open surgical repair among patients with abdominal aortic aneurysms under surveillance. J. Vasc. Surg. 49 (3), 576–581.e573.

Zovatto, L., Pedrizzetti, G., 2018. Optimal helical entry flow in a helical vessel. Fluid Dyn. Res. 50, (6) 065503.